Bioactive Materials 14 (2022) 76–85

Contents lists available at ScienceDirect

Bioactive Materials

journal homepage: www.keaipublishing.com/en/journals/bioactive-materials

2D-ultrathin MXene/DOXjade platform for iron chelation chemo-photothermal therapy

Yunjie Xu [a,b,1], Yingwei Wang [e,1], Jusung An [b,1], Adam C. Sedgwick [d,1], Mingle Li [b], Jianlei Xie [a], Weibin Hu [c], Jianlong Kang [a], Sajal Sen [d], Axel Steinbrueck [d], Bin Zhang [f], Lijun Qiao [c], Swelm Wageh [g], Jonathan F. Arambula [d,*], Liping Liu [c,**], Han Zhang [a,***], Jonathan L. Sessler [d,****], Jong Seung Kim [b,*****]

[a] Shenzhen Engineering Laboratory of Phosphorene and Optoelectronics; International Collaborative Laboratory of 2D Materials for Optoelectronics Science and Technology of Ministry of Education, Shenzhen Institute of Translational Medicine, Department of Otolaryngology, Shenzhen Second People's Hospital, The First Affiliated Hospital, College of Optoelectronic Engineering, Shenzhen University, Shenzhen, 518060, China
[b] Department of Chemistry, Korea University, Seoul, 02841, South Korea
[c] Department of Hepatobiliary and Pancreatic Surgery, Shenzhen People's Hospital, Second Clinical Medical College of Jinan University, Shenzhen, 518020, China
[d] Department of Chemistry, The University of Texas at Austin, Austin, TX, 78712-1224, USA
[e] Hunan Key Laboratory of Nanophotonics and Devices, School of Physics and Electronics, Central South University, 932 South Lushan Road, Changsha, 410083, China
[f] Institute of Translation Medicine Shenzhen Second People's Hospital First Affiliated Hospital of Shenzhen University, Shenzhen, 518035, China
[g] Department of Physics, Faculty of Science, King Abdulaziz University, Jeddah, 21589, Saudi Arabia

ARTICLE INFO

Keywords:
2D MXene
Nanomedicine
Prodrug
Iron chelation
Photothermal therapy

ABSTRACT

An increased demand for iron is a hallmark of cancer cells and is thought necessary to promote high cell proliferation, tumor progression and metastasis. This makes iron metabolism an attractive therapeutic target. Unfortunately, current iron-based therapeutic strategies often lack effectiveness and can elicit off-target toxicities. We report here a dual-therapeutic prodrug, **DOXjade**, that allows for iron chelation chemo-photothermal cancer therapy. This prodrug takes advantage of the clinically approved iron chelator deferasirox (ExJade®) and the topoisomerase 2 inhibitor, doxorubicin (DOX). Loading **DOXjade** onto ultrathin 2D Ti_3C_2 MXene nanosheets produces a construct, **Ti_3C_2-PVP@DOXjade**, that allows the iron chelation and chemotherapeutic functions of **DOXjade** to be photo-activated at the tumor sites, while potentiating a robust photothermal effect with photothermal conversion efficiencies of up to 40%. Antitumor mechanistic investigations reveal that upon activation, **Ti_3C_2-PVP@DOXjade** serves to promote apoptotic cell death and downregulate the iron depletion-induced iron transferrin receptor (TfR). A tumor pH-responsive iron chelation/photothermal/chemotherapy antitumor effect was achieved both *in vitro* and *in vivo*. The results of this study highlight what may constitute a promising iron chelation-based phototherapeutic approach to cancer therapy.

1. Introduction

Cancer remains one of the most serious diseases affecting the global population [1–3]. Despite major therapeutic breakthroughs in recent decades, cancer incidence remains high. Moreover, most available treatment options fail to suppress reliably the development of chemoresistance as well as cancer reoccurrence [1]. Current treatments are also plagued by limited tumor specificity and unwanted off-target

Peer review under responsibility of KeAi Communications Co., Ltd.
* Corresponding author.
** Corresponding author.
*** Corresponding author.
**** Corresponding author.
***** Corresponding author.
E-mail addresses: jfarambula@cm.utexas.edu (J.F. Arambula), leoliping@aliyun.com (L. Liu), hzhang@szu.edu.cn (H. Zhang), sessler@cm.utexas.edu (J.L. Sessler), jongskim@korea.ac.kr (J.S. Kim).
[1] Those authors contributed equally to this work.

https://doi.org/10.1016/j.bioactmat.2021.12.011
Received 24 September 2021; Received in revised form 26 November 2021; Accepted 13 December 2021
Available online 18 December 2021

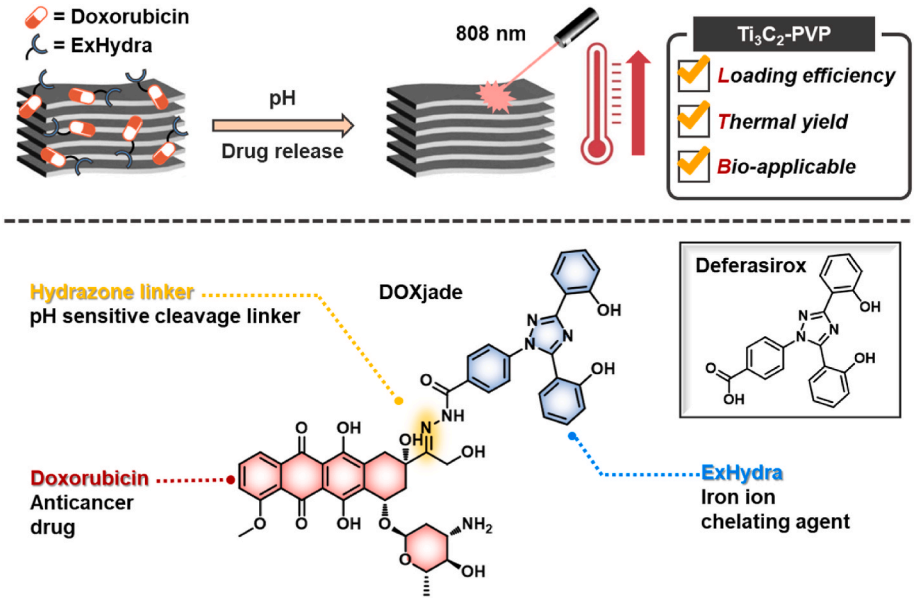

Scheme 1. Schematic representation of **DOXjade** being loaded onto 2D ultrathin Ti_3C_2 MXene nanosheets to create constructs that allow for combined iron chelation chemo-photothermal therapy.

cytotoxicity, limitations that can lead to side effects such as nausea, vomiting, hair loss and increased susceptibility towards bleeding and infections [4]. To address these challenges, new advanced anticancer treatments are urgently needed.

Iron chelation therapy has gained increasing attention in recent years as a potential primary or adjuvant cancer treatment option [5–7]. Iron is an essential element for humans and access to iron is an absolute requirement for cellular proliferation [8]. In general, the cellular iron pool is well-balanced and is dynamically regulated by certain transmembrane proteins, such as ferroportin 1 [9]. However, owing to the rapid synthesis of DNA during cell growth, cancer cells exhibit an abnormal iron metabolism with higher demand for iron than normal cells, as reflected, for instance, in the upregulation of the iron uptake protein transferrin receptor (TfR) in various types of cancers [10,11]. As a consequence, tumor cells are more sensitive to iron deprivation. This, in turn, makes selective modulation of cellular iron metabolism a promising approach to cancer chemotherapy drug development [10]. One notable system of interest in this context is the FDA-approved iron chelating agent deferasirox (ExJade®, Scheme 1) [12,13], which has been shown to exert inhibitory effects towards cancer cells *in vitro* and *in vivo* models derived from human liver, lung and pancreatic cells. Promising preliminary success in the treatment of a patient with acute myelogenous leukemia has also been reported [14–16]. Unfortunately, dose-dependent toxicity and non-targeting issues constitute roadblocks in the clinical development of deferasirox for cancer-related indications.

A promising approach to improve the therapeutic efficacy of deferasirox would be to make it part of a combination therapy. Here, the idea, as with other so-called drug cocktails, is to exploit multiple therapeutic strategies simultaneously to increase synergistically the anticancer activity of the individual treatments without reaching their respective dose-limiting toxicities [17–21]. One modality that appears attractive for combination with deferasirox is photothermal therapy (PTT), which relies on photonic energy to generate local hyperthermia to damage cancer cells [22–24]. PTT takes advantage of the susceptibility of cancer cells toward heat to induce apoptosis [25,26]. Especially, because of its O_2-independent mechanism of action, PTT has emerged as an important strategy for improving the sensibility of conventional cancer treatments, such as radio- and chemotherapy [27–30]. We therefore postulated that rationally designed photothermal systems that include an iron chelation element would prove promising in terms of combating malignant tumors. Unfortunately, simple combination strategies, such as those that rely on, e.g., direct loading of an active drug form into nanocomposites, usually do not address the problem of off-target toxicities that plague traditional cancer treatments.

Considering the limitations in combination therapy, we sought to develop a "dual-therapeutic prodrug nanomedicine" approach involving iron chelation chemo-photothermal therapy as illustrated in Scheme 1. Here, the key elements are 1) a new tumoral acid microenvironment responsive dual-therapeutic conjugate (**DOXjade**) that incorporates in one molecular construct both the iron chelator deferasirox and the clinically approved topoisomerase 2 inhibitor, doxorubicin (DOX), and 2) ultrathin two-dimensional (2D) Ti_3C_2 MXene nanosheets designed to act as a photothermal generator and drug delivery carrier. The two drug components making up **DOXjade** are tethered through a pH-sensitive linker, namely a hydrazone bond (Scheme 1). Our design expectation was that the choice of an acid-labile hydrazone linker would enable the inherent iron chelation and chemotherapeutic functions of **DOXjade** to be activated preferentially at tumor sites, thereby reducing off-target toxicity effects.

Nanomaterials, especially those with good biocompatibility and drug loading efficiencies, are attracting increasing attention within the context of cancer nanomedicine [31–36]. As an emerging member of 2D material family, Ti_3C_2 MXene nanosheets showed several advantages for nanocarrier biomedicine application including significant light absorbed ability in near infrared (NIR) light, large specific surface area and excellent air-stability and solution stability [32]. In this context, 2D ultrathin Ti_3C_2 MXene nanosheets, benefitting from a planar structure with a large surface area, were expected to interact strongly with **DOXjade**. The resulting construct, termed **Ti_3C_2-PVP@DOXjade**, was, in turn, expected to display good photothermal efficiency [37]. In fact, as detailed below, the Ti_3C_2 nanosheets present in **Ti_3C_2-PVP@DOXjade** displayed photothermal conversion efficiencies of up to 40% and provided excellent PTT performance when subject to NIR light irradiation at 808 nm within the so-called "optical-therapeutic window (650–900 nm)" [38,39]. Moreover, a sensitive tumor pH-responsive iron chelation/PTT/chemotherapy antitumor effect was seen with **Ti_3C_2-PVP@DOXjade**.

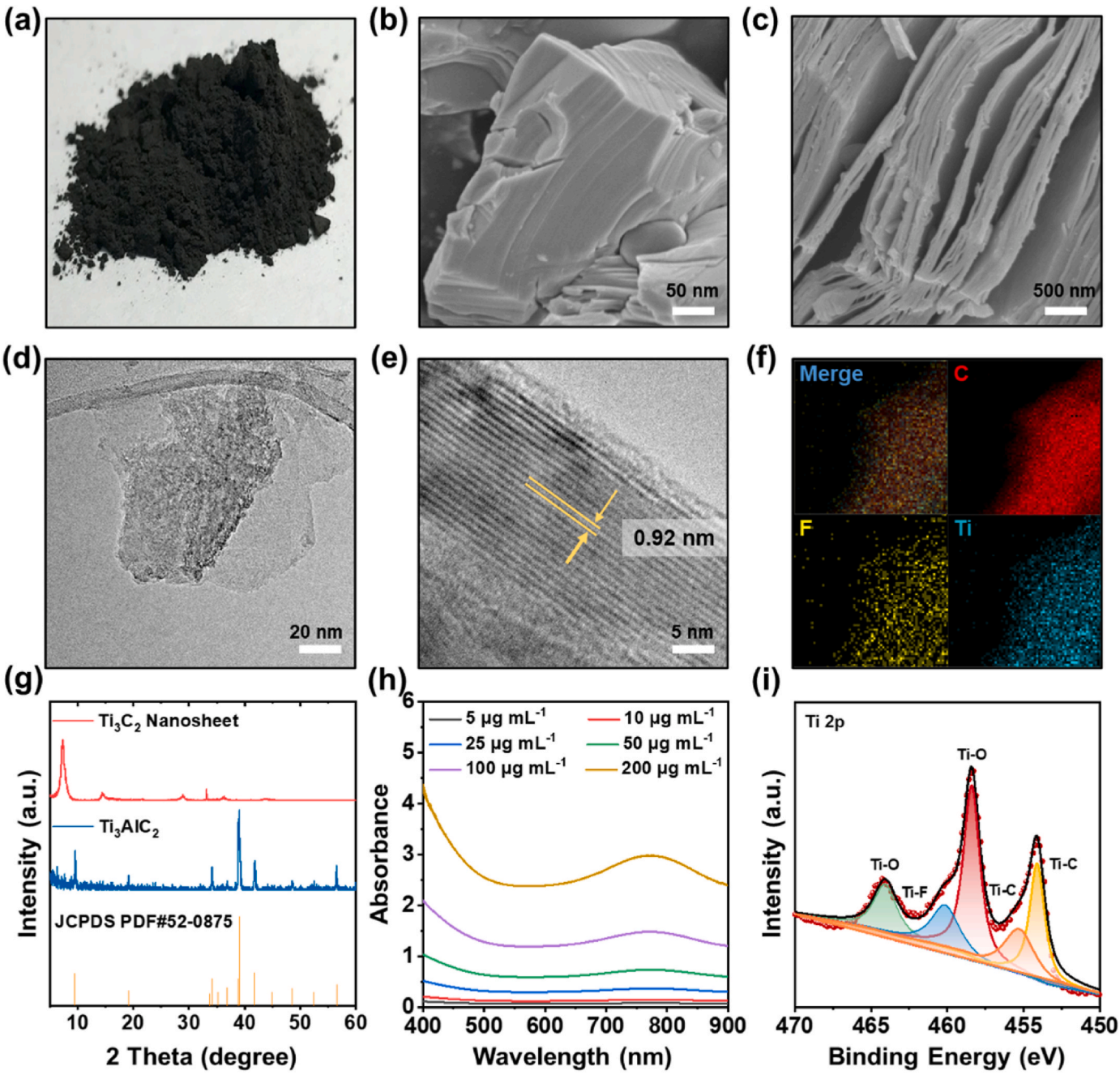

Fig. 1. Characterization of Ti_3AlC_2 MAX phase and Ti_3C_2 nanosheets. a) Digital photograph and b) SEM image of bulk Ti_3AlC_2. c) SEM images of multilayer Ti_3C_2. d) TEM images of the Ti_3C_2 nanosheets. e) Cross-sectional TEM image of the Ti_3C_2 nanosheets. f) EDS elemental mapping results of theTi_3C_2 nanosheets. g) The XRD patterns of theTi_3C_2 nanosheet (red graph) and bulk Ti_3AlC_2 (blue graph). h) UV–vis absorption spectrum of Ti_3C_2 nanosheets at different concentrations in deionized water. i) High-resolution XPS spectra of the Ti 2p orbital.

2. Results and discussion

2.1. Synthesizes and Characterization of Ti_3C_2 nanosheets

Ti_3C_2 nanosheets were synthesized *via* a hydrofluoric acid (HF) etching method (see Methods section for full details). Bulk Ti_3AlC_2 powder was initially ground into a fine black powder (400 mesh) (Fig. 1a). As revealed by scanning electron microscope (SEM) images, the bulk Ti_3AlC_2 MAX phase consists of layered Ti_3C_2 and planar aluminum (Al) atomic sheets (Fig. 1b). HF etching was then used to remove the atomic Al sheets and facilitate the formation of a multilayer Ti_3C_2 material with a typical "accordion" morphology (Fig. 1c). After intercalation and sonication, delaminated Ti_3C_2 nanosheets with a thin and transparent structure were obtained, as confirmed by transmission electron microscopy (TEM) (Fig. 1d). As shown in Fig. 1e, cross-sectional TEM images of the stacked layers of Ti_3C_2 revealed interlayer distances of 9.2 Å, which is in good agreement with previous reports [37,40,41]. Scanning transmission electron microscopy (STEM) with energy dispersive X-ray spectroscopy (EDS) was used to detect the presence of Ti, C and F, as well as the excellent overlap of these three elements (Fig. 1f). The fluorine atoms present in the sample presumably originate from the HF etching and exist on the surface of Ti_3C_2 sheets as surface terminating moieties. The X-ray diffraction (XRD) patterns of the Ti_3AlC_2 samples prepared as above (Fig. 1g) proved to be in agreement with the Joint Committee on Powder Diffraction Standards (JCPDS PDF#52–0875). This was taken as evidence that the crystallinity of

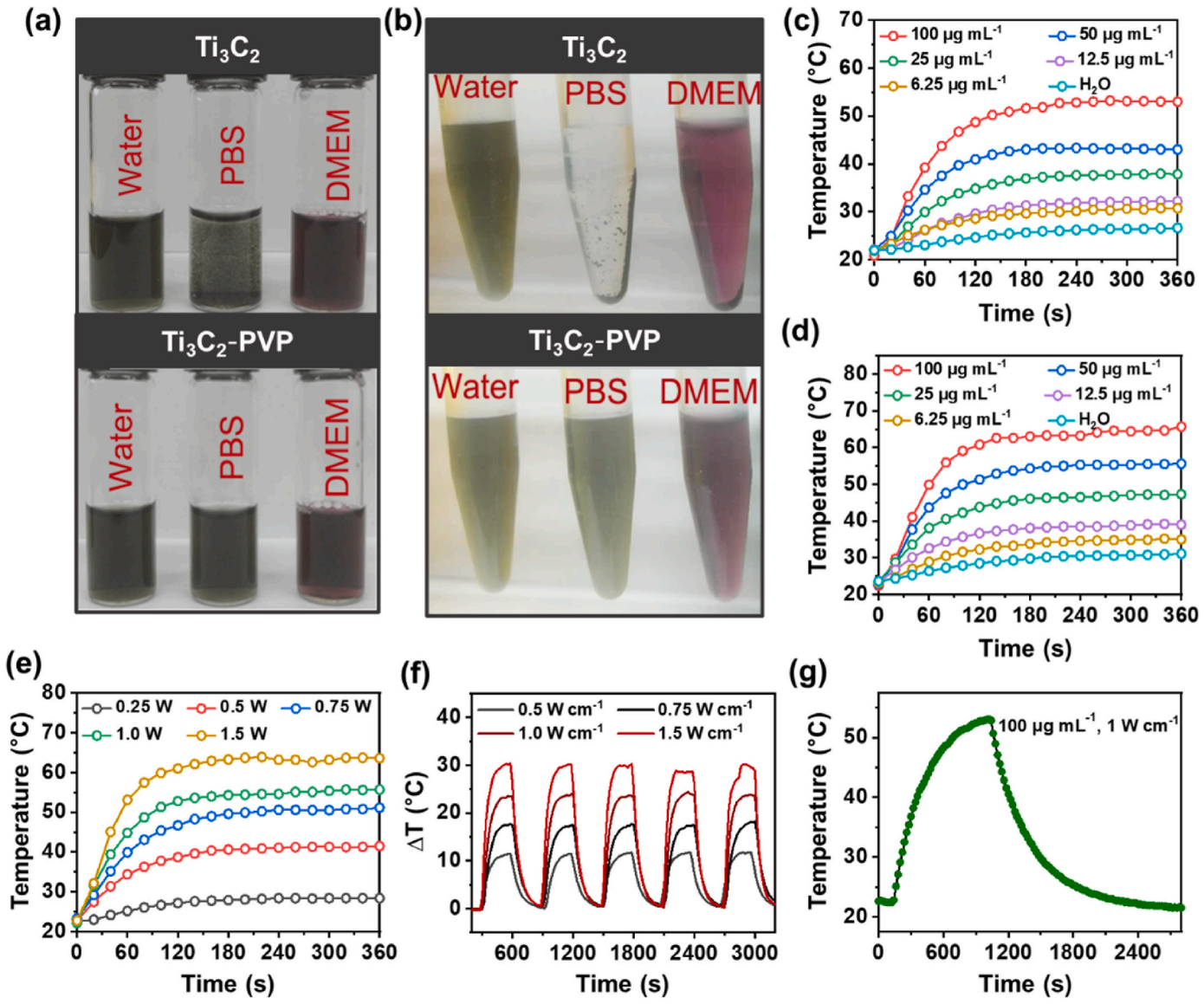

Fig. 2. Photothermal performance and stability studies of Ti_3C_2 nanosheets in different media. a) Photographs of aqueous solutions of Ti_3C_2 and Ti_3C_2-PVP nanosheets dispersed in different solvents (water, PBS and DMEM). b) Photographs of Ti_3C_2 and Ti_3C_2-PVP nanosheets after centrifugation at 3000 rpm. Photothermal performance of different concentrations of Ti_3C_2-PVP under laser irradiation intensities of c) 1 W cm^{-2} and d) 1.5 W cm^{-2}. e) Photothermal performance of Ti_3C_2-PVP (100 μg mL^{-1}) under different laser irradiation intensities. f) Temperature change curves for Ti_3C_2-PVP (100 μg mL^{-1}) dispersed in deionized water after five laser on/off cycles under different laser irradiation intensities. g) Photothermal effect of Ti_3C_2-PVP under 808 nm photo-irradiation showing one heating and cooling cycle.

Ti_3AlC_2 MAX phase is maintained. In comparison to bulk Ti_3AlC_2, the most intense peak at 39° 2θ was absent in the case of the Ti_3C_2 nanosheets (Fig. 1g), which was ascribed to exfoliation [40]. Moreover, the (002) peaks at 9.6° in the original Ti_3AlC_2 samples were found to shift to a lower angle (7.2°) in the case of the Ti_3C_2 nanosheets. Broadening of this peak was also seen (Fig. 1g). These are typical features of Ti_3C_2. The UV–vis absorption spectrum of Ti_3C_2 was shown to have a noticeable and broad absorption in the visible and NIR region (600–900 nm), which is attributed to a surface plasmon resonance of Ti_3C_2 (Fig. 1h) [37]. The results of high-resolution XPS analyses of the Ti 2p region are shown in Fig. 1i and fittings of the Ti 2p peaks proved consistent with previous reports [42]. Binding energies of 459.3 eV and 465.1 eV were assigned to the Ti–O bonds in TiO_2, while the peaks corresponding to the Ti–C bonds in Ti_3C_2 were found to have binding energies of 454.1 eV and 455.5 eV, respectively. The peak at a binding energy of 461.6 eV is assigned to the Ti–F bond, further substantiating the formation of Ti–F bonds as surface termination moieties. The XPS spectra of the Ti_3C_2 nanosheets (Fig. S1a) displayed four peaks assigned to the F 1s, O 1s, Ti 2p and C 1s orbitals, respectively, reflecting the main elements found in the Ti_3C_2 nanosheets. Fitting the high-resolution XPS spectra of the O 1s orbital provided support for overlap between the O–Al, O–H and O–Ti bonds (Fig. S1b). High resolution XPS spectra of the Al 2p orbital in Ti_3C_2 and Ti_3AlC_2 are shown in Fig. S1c. Importantly, the peak corresponding to the Al 2p orbital was absent in the case of the Ti_3C_2 sample, which was taken as evidence for the removal of Al atoms from Ti_3AlC_2 during the synthesis of Ti_3C_2. Atomic force microscopy (AFM) was used to investigate the thickness of the Ti_3C_2 sheets, giving an average height of 6.07 ± 2.7 nm, which corresponds to the thickness expected for a few Ti_3C_2 nanosheet layers (Fig. S2) [37].

2.2. Surface functionalization and the photothermal performance of Ti_3C_2 nanosheets

For 2D nanomaterials to be used in drug delivery and

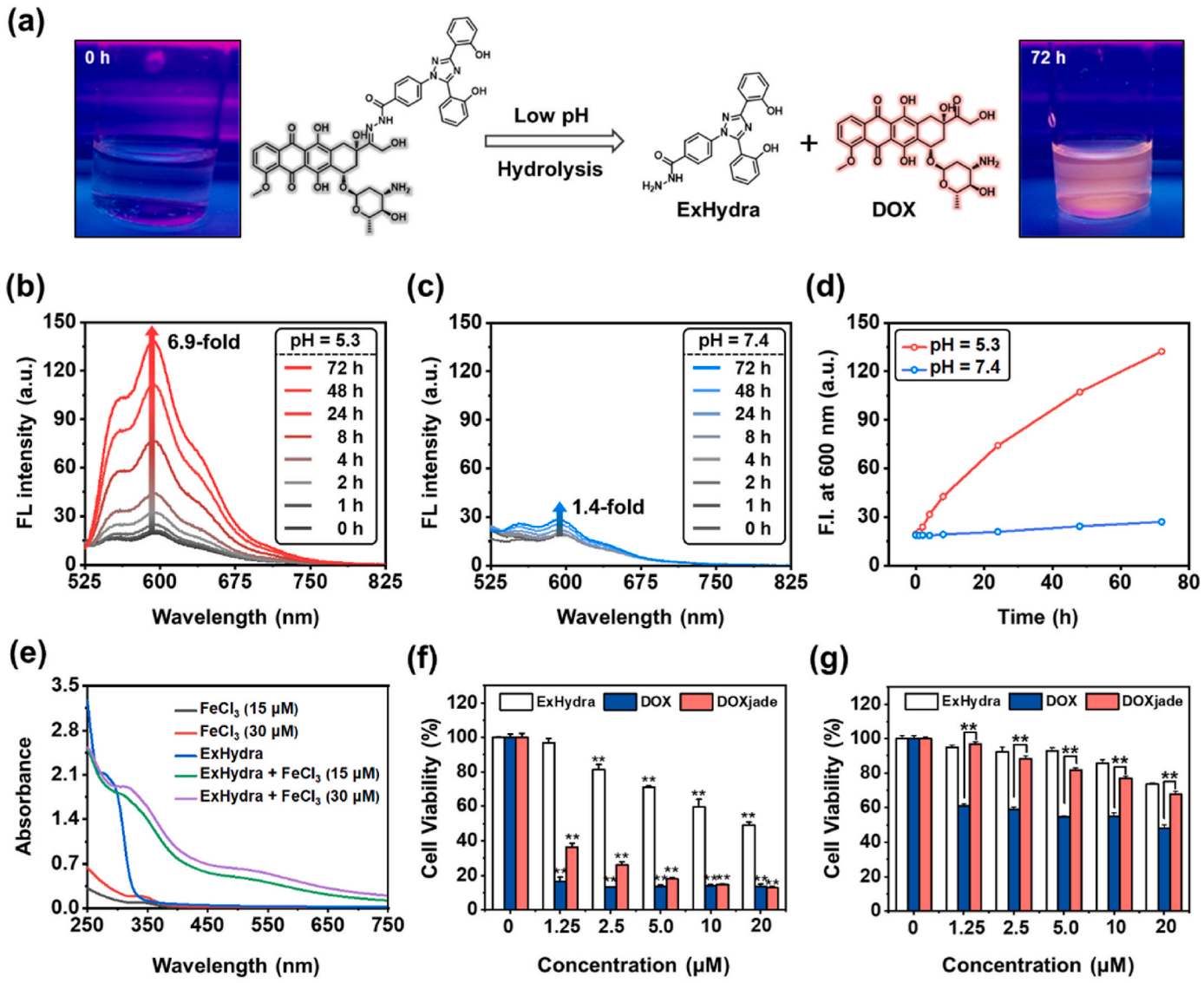

Fig. 3. Hydrolysis of **DOXjade** seen at low pH and results of cytotoxicity assays carried out with DOX, ExHydra and **DOXjade**. (a) Scission of **DOXjade** (hydrazone bond cleavage) results in a fluorescence 'turn-on' response and concurrent release of both drugs (ExHydra and DOX). (b) Fluorescence spectra of **DOXjade** (10 μM) recorded as a function of time (0–72 h) in acetate buffer (pH = 5.3), and (c) PBS buffer (pH = 7.4). λ_{ex} = 500 nm. Slit widths: ex = 10 nm and em = 10 nm. (d) Relative fluorescence intensity changes of aqueous samples of **DOXjade** at λ_{em} = 600 nm as a function of time (0–72 h); data are derived from (b) and (c). (e) Absorbance profiles of ExHydra (30 μM), $FeCl_3$ (30 μM), alone and in combination in acetate buffer at pH = 5. The interaction between ExHydra and Fe^{3+} is inferred based on analogy to deferasirox and is supported by the observation of a broad band at around 510 nm. (f) Viability of human colorectal cancer cells HCT116 seen upon incubation with different concentrations of ExHydra, DOX and **DOXjade**, as determined from CCK-8 assays. (g) Dose dependent cytotoxicity of ExHydra, DOX and **DOXjade** towards HMEC-1 cells. Mean ± SD (n = 3). $^{**}p < 0.01$ *vs.* control.

phototherapeutic applications, solution stability and biocompatibility are required. Ti_3C_2 synthesized *via* acid etching affords a negatively charged surface due to the presence of hydroxyl and fluorine units anchored to the surface [43,44]. This negative surface charge affords acid etched Ti_3C_2 nanosheets with good stability in aqueous media. Unfortunately, in the presence of positively charged ions, such as those present as counter cations in phosphate buffered saline (PBS) and Dulbecco's modified eagle medium (DMEM), aggregation or precipitation of Ti_3C_2 occurs as shown in Fig. 2a. To address this issue, we subjected our etched Ti_3C_2 to surface functionalization with polyvinylpyrrolidone (PVP) (Methods section). The resulting material, Ti_3C_2-PVP, as well as Ti_3C_2 and PVP, were characterized by Fourier transform infrared spectroscopy (FTIR) (Fig. S3a). PVP displayed infrared absorption peaks ascribable to the expected C–O, C–N, $–CH_2$ functionalities. This observation was taken as evidence that PVP had been anchored successfully onto the Ti_3C_2 nanosheets. Dynamic laser scattering (DLS) analyses revealed that the Ti_3C_2-PVP nanosheets were larger than the unfunctionalized Ti_3C_2 nanosheets (Fig. S3b), as expected for a functionalized system. The aqueous stability of the Ti_3C_2-PVP nanosheets was evaluated in PBS and DMEM solution (Fig. 2b). No discernible aggregation was observed when Ti_3C_2-PVP was subjected to centrifugation at 3000 rpm for 5 min. In contrast, under the same conditions, unfunctionalized Ti_3C_2 nanosheets aggregated. We thus suggest that Ti_3C_2-PVP is appropriate for use in biological studies.

The photothermal performance of Ti_3C_2-PVP was then evaluated. In these studies, different concentrations of Ti_3C_2-PVP were subject to 808 nm laser irradiation at 1 W cm^{-2} (Fig. 2c) and 1.5 W cm^{-2} (Fig. 2d), respectively. Ti_3C_2-PVP displayed excellent photothermal properties. For instance, with irradiation at 1.5 W cm^{-2} for 360 s, a 100 μg mL^{-1} solution in Ti_3C_2-PVP reached a temperature of 63 °C (Fig. 2d). A concentration dependence was seen for these photoinduced temperature changes (Fig. 2e). To test the photostability of Ti_3C_2-PVP, Ti_3C_2-PVP

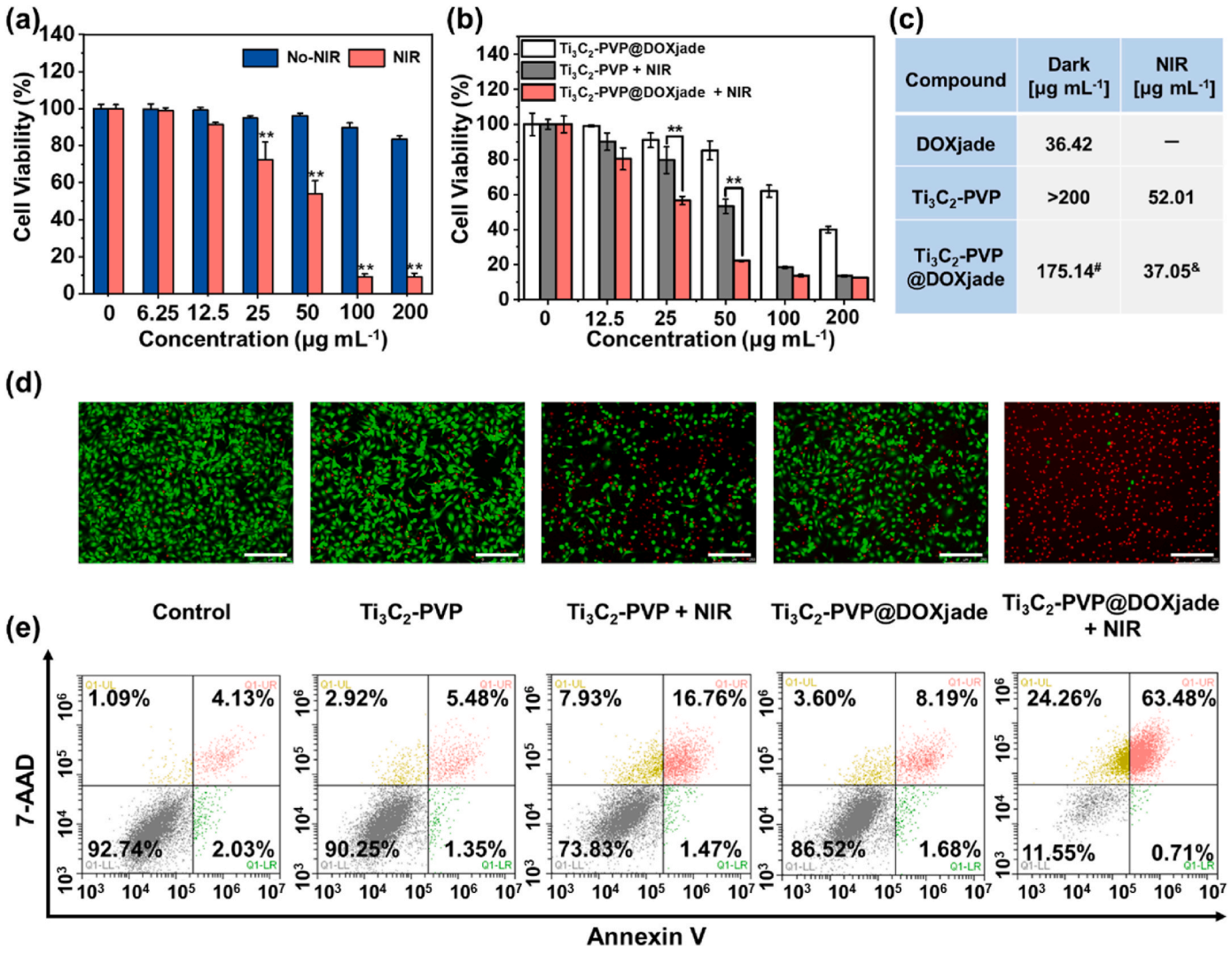

Fig. 4. *In vitro* photothermal effects produced upon subjecting Ti_3C_2-PVP to photo-irradiation. (a) Relative cell viabilities of HCT116 cells treated with different concentrations of Ti_3C_2-PVP and exposed to laser irradiation at 808 nm for 10 min. (b) Relative cell viabilities of HCT116 cells treated with Ti_3C_2-PVP, **Ti_3C_2-PVP@DOXjade** with or without exposure to laser irradiation (808 nm). (c) IC_{50} values deduced from studies of HCT116 cells treated with **DOXjade**, Ti_3C_2-PVP, **Ti_3C_2-PVP@DOXjade** with or without NIR exposure. Note the concentration differences: #175.14 μg mL^{-1} **Ti_3C_2-PVP@DOXjade** (Ti_3C_2-PVP: 141.88 μg mL^{-1}; **DOXjade**: 33.25 μg mL^{-1}); &37.05 μg mL^{-1} **Ti_3C_2-PVP@DOXjade** (Ti_3C_2-PVP: 30.02 μg mL^{-1}; **DOXjade**: 7.03 μg mL^{-1}). (d) Fluorescent images of live/dead HCT116 cells stained using calcein AM (green, live cells) and propidium iodide (red, dead cells) after addition of Ti_3C_2-PVP (40.51 μg mL^{-1}), **Ti_3C_2-PVP@DOXjade** 50 μg mL^{-1} (Ti_3C_2-PVP: 40.51 μg mL^{-1}; **DOXjade**: 9.49 μg mL^{-1}) with or without laser irradiation (1 W cm^{-2}). (Scale bars: 250 μm) (e) Representative annexin V-FITC/7-AAD scatter plots for HCT116 cells treated as in (d). Mean ± SD (n = 3). *$p < 0.05$, **$p < 0.01$ *vs.* control.

solutions were subject to NIR laser radiation (laser on) followed by natural cooling back to room temperature (laser off) for five on/off cycles. As inferred from the associated temperature change profiles, no discernible degradation was observed. Similar results were seen at different power settings (Fig. 2f). On this basis we conclude that Ti_3C_2-PVP would prove stable under conditions of photo-activation *in vivo*.

To determine the photothermal conversion efficiency (η) of Ti_3C_2-PVP, the temperature change was recorded under NIR laser radiation for 10 min (laser on) followed by natural cooling to room temperature (laser off) as seen in Fig. 2g. The time constant for heat transfer from the system was determined to be 310 s by plotting the linear time data from the cooling period versus the negative natural logarithm of the driving force temperature, as shown in Fig. S4. Using conventional methods [32, 37], the η value for Ti_3C_2-PVP was determined to be 40%, highlighting the potential of Ti_3C_2-PVP as a possible PTT agent for cancer treatment.

2.3. Drug (*DOXjade*) loading onto the Ti_3C_2 nanosheets

The dual-therapeutic agent, **DOXjade,** was synthesized *via* the acid mediated (trifluoroacetic acid, TFA) condensation between a hydrazide functionalized deferasirox derivative (ExHydra) and DOX (see Methods for full synthesis) - Scheme S1. Ti_3C_2-PVP and **DOXjade** were then mixed in PBS. **DOXjade** was added at different feeding ratios, set at 1.0, 1.5 2.0, 2.5 and 3.0, respectively, and stirred overnight under an inert atmosphere. As shown in Fig. S3b, after anchoring **DOXjade** to the surface of Ti_3C_2-PVP, the resulting **Ti_3C_2-PVP@DOXjade** constructs were larger than Ti_3C_2-PVP, as evidenced by DLS. The loading of **DOXjade** onto Ti_3C_2-PVP (to give **Ti_3C_2-PVP@DOXjade**) resulted in a change in the zeta potential from negative to positive (Fig. S3c). This finding provides further support for the suggestion that **DOXjade** was successfully loaded onto the Ti_3C_2-PVP nanosheets.

To determine the drug loading capacity of Ti_3C_2-PVP, we first recorded a standard concentration-absorbance curve for **DOXjade** at 440 nm (Fig. S5a). Presumably as a consequence of their planar

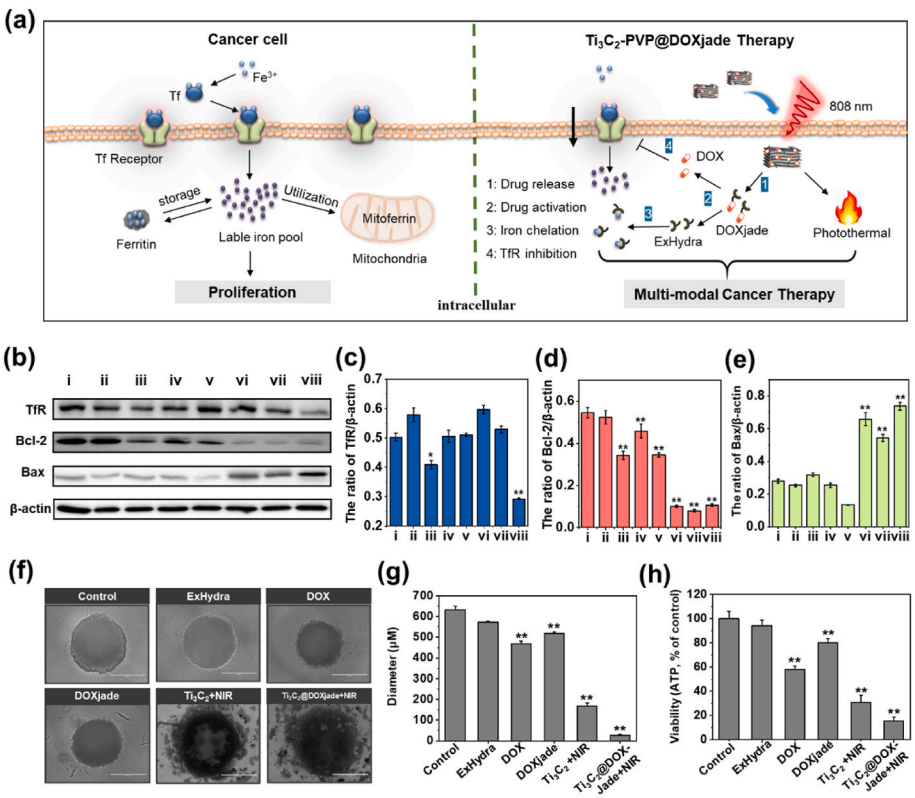

Fig. 5. Antitumor mechanistic studies of **Ti_3C_2-PVP@DOXjade**-based treatment. (a) Scheme showing key events. 1: **DOXjade** is released from Ti_3C_2-PVP; 2: Hydrolysis of **DOXjade** into DOX and ExHydra; 3: Iron chelation by ExHydra; 4: Inhibition of TfR expression by DOX. Tf: Transferrin Receptor. (b) Western blot analysis of the expression of the iron metabolism related protein TfR and the Bcl-2 and Bax proteins involved in apoptosis in HCT-116 cells after drug administration and laser irradiation. In this and other applicable panels, i: Control; ii: ExHydra; iii: DOX; iv: **DOXjade**; v: Ti_3C_2-PVP; vi: Ti_3C_2-PVP + NIR; vii: **Ti_3C_2-PVP@DOXjade**; viii: **Ti_3C_2-PVP@DOXjade** + NIR; quantitation of TfR (c) Bcl-2 (d), and Bax (e) protein levels. Morphology (f) and diameter (g) analyses of 3D tumor spheroid cultures of HCT-116 cells after being incubated for 72 h with ExHydra, DOX, or **DOXjade**. Scale bar 400 μm. (h) Results of spheroid viability expressed as a percentage with the value for the negative control cells arbitrarily set at 100%. NIR laser = 808 nm, 1.0 W cm^{-2}, 10 min. Mean ± SD (n = 3). $^*p < 0.05$, $^{**}p < 0.01$ *vs.* control.

structure and large surface area [32], the present 2D ultrathin MXene Ti_3C_2-PVP nanosheets exhibited a loading potency for **DOXjade** of 210% (Fig. S5b). This relatively high drug loading efficiency was viewed as being advantageous since it was expected to allow **DOXjade** to be delivered efficiently to tumor sites via, e.g., a classic EPR (enhanced permeability and retention) effect, while minimizing potentially non-specific accumulation within normal tissues.

2.4. *pH-triggered drug release and cytotoxicity of **DOXjade***

In accord with our design expectations, **DOXjade** was found to hydrolyze into its respective components (DOX and ExHydra) under acidic conditions (Fig. 3a), as inferred from LC-MC analyses (Figs. S17–S19). This cleavage was found to occur in a pH-dependent manner. As shown in Fig. 3b, in acetate buffer (pH = 5.3), the maximum intensity of the fluorescence emission feature ascribed to DOX at 600 nm increased in a time-dependent manner (0–72 h) to a maximum of 6.9-fold. In contrast, in neutral medium (pH = 7.4), the intensity of the 600 nm emission feature increased by only 1.4-fold under otherwise identical conditions (Fig. 3c and d). These results provide support for a key hypothesis underlying the present study, namely that **DOXjade** would be able to act as a prodrug capable of releasing its two constituents, ExHydra and DOX in acidic tumor microenvironments. ExHydra possesses the same chelating motif as deferasirox and it was found to display near-identical UV–vis spectral changes when exposed to Fe (III) (Fig. 3e). Thus, the mode of action of ExHydra was assumed to be the same as deferasirox [45].

Cell proliferation assays were conducted to evaluate the cytotoxicity of **DOXjade**, DOX and ExHydra in cancer cell lines and human normal cells. The results of a cell counting kit-8 (CCK-8) cell viability assay revealed that DOX and **DOXjade** inhibited cancer cells growth more effectively than ExHydra alone. In the human colorectal cancer cell lines (SW480, HCT116, DLD1) and the hepatocellular carcinoma cell lines (HepG2, Huh-7), tumor cell growth was inhibited by **DOXjade** in a dose and time dependent manner (Fig. 3f and S6). However, in normal human mammary epithelial HMEC-1 cells, **DOXjade** displayed a markedly lower cytotoxicity as compared to free DOX and ExHydra (Fig. 3g), leading us to suggest that our dual-therapeutic prodrug design would display reduced off-target toxicity when tested *in vivo*.

2.5. *Iron chelation chemo-photothermal therapy in vitro*

We then evaluated the iron chelation chemo-photothermal efficiency of **Ti_3C_2-PVP@DOXjade** in HCT116 cells using the CCK-8 assay. Ti_3C_2-PVP and **DOXjade** were included as controls. The 2D ultrathin Ti_3C_2-PVP nanosheets exhibited satisfactory biocompatibility and potent PTT efficiency in cells. For instance, after incubating Ti_3C_2-PVP in cells for 6 h, negligible cytotoxicity was noted even at concentrations up to 200 μg mL^{-1} (Fig. 4a and S7). In contrast, an IC_{50} (half maximal inhibitory concentration) of 52.01 μg mL^{-1} was recorded upon subjecting Ti_3C_2-PVP to 808 nm laser irradiation for 10 min (1 W cm^{-2}), (Fig. 4c). This finding, which is consistent with a previous report [46], provided us with support for the notion that Ti_3C_2-PVP would serve as an effective PTT platform for use in conjunction with **DOXjade**. Studies of **Ti_3C_2-PVP@DOXjade** were thus carried out under conditions identical to those used in the case of Ti_3C_2-PVP (808 nm, 1 W cm^{-2}, 10 min). This yielded an IC_{50} value of 37.05 μg mL^{-1} (Ti_3C_2-PVP: 30.02 μg mL^{-1}; **DOXjade**: 7.03 μg mL^{-1}) (Fig. 4b), representing a 5.2- and 1.7-fold improvement relative to **DOXjade** and PTT (Ti_3C_2-PVP + NIR) treatments, respectively (Fig. 4c). These improvements are ascribed to a **DOXjade** dual-therapeutic effect (iron chelation and chemotherapy) that complements that provided by Ti_3C_2-PVP-mediated PTT. Live/dead cell staining using a calcein AM/7-AAD assay kit, in which the live cells produce a green fluorescence while dead cells give rise to a red fluorescence [47,48], provided support for the inference that efficient tumor cells damage is engendered as the result of the putative combination treatment (Fig. 4d). For instance, FACS analysis revealed Annexin V-FITC/7-AAD (7-aminoactinomycin D) staining for the majority of the HCT116 cells subject to photo-irradiation (Fig. 4e) reflecting an increase in cellular apoptosis.

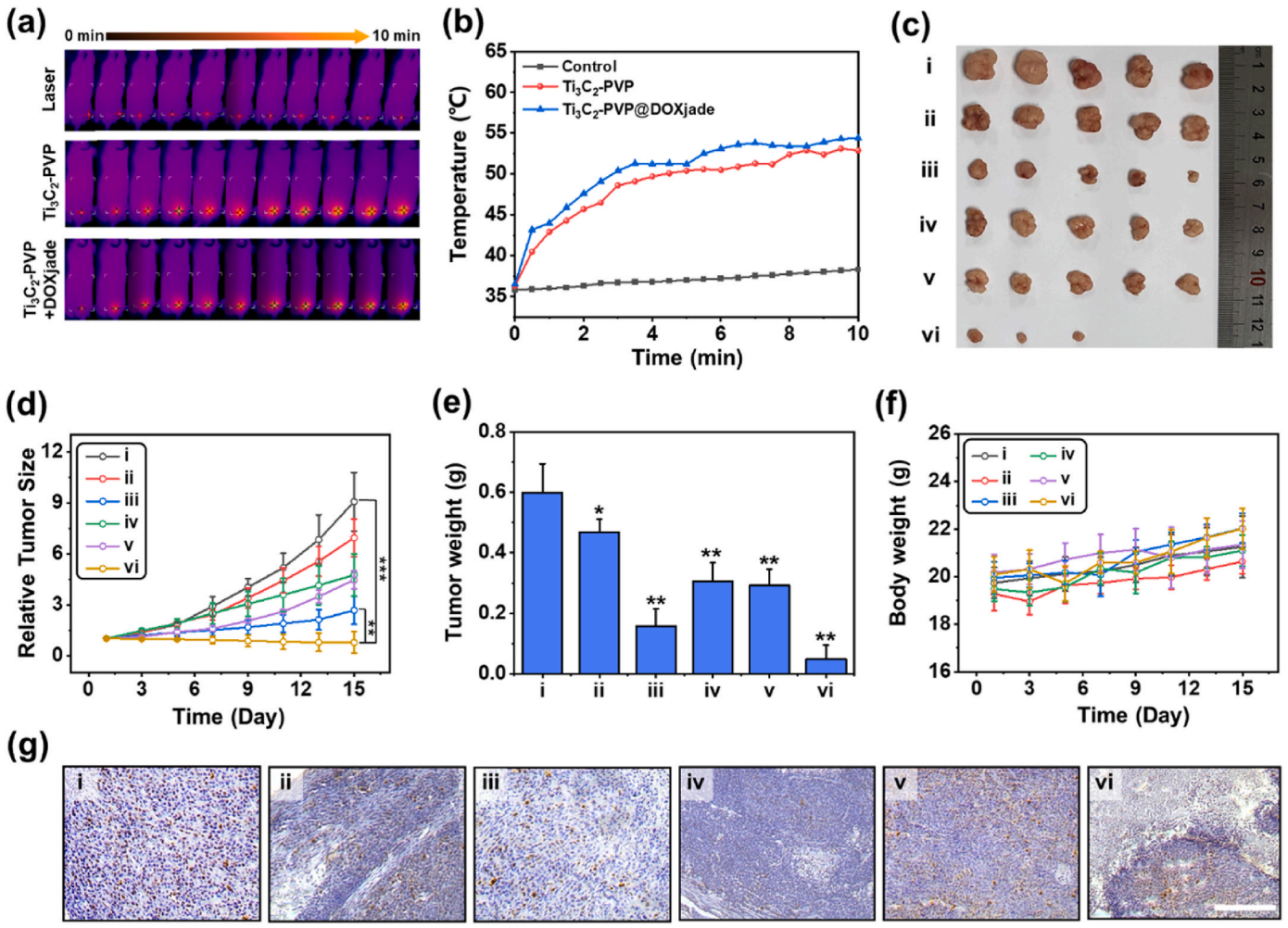

Fig. 6. *In vivo* NIR imaging and antitumor effect of **Ti_3C_2-PVP@DOXjade**. (a) Thermal images of mice bearing tumors after injection with Ti_3C_2-PVP or **Ti_3C_2-PVP@DOXjade**, followed by exposure to 808 nm laser irradiation (1.0 W cm^{-2}, 10 min). (b) Changes in tumor temperature seen in mice bearing HCT116 tumors upon laser irradiation. (c) Morphology of tumors removed from mice sacrificed at the end point of the study. Groups in this and the other studies in this figure are as follows: i: Control; ii: ExHydra; iii: DOX; iv: **DOXjade**; v: Ti_3C_2-PVP + NIR; vi: **Ti_3C_2-PVP@DOXjade** + NIR, where NIR denotes laser irradiation (808 nm, 1.0 W cm^{-2}, 10 min). (d) Inhibition of HCT116 tumor growth seen upon different treatments. (e) Weight of tumors excised from BALB/c nude mice involved in this study. (f) Body weight of BALB/c nude mice recorded every two days for two weeks after intravenous injection of the indicated agents. (g) Tumor growth inhibition as analyzed by Ki67 staining of tumor tissues. Scale bar: 200 μm. Mean ± SD (n = 5). $^{**}p < 0.01$, $^{***}p < 0.001$ *vs.* control.

2.6. Antitumor mechanistic analyses

Encouraged by the antitumor efficiency observed *in vitro*, we further studied the working mechanism of **Ti_3C_2-PVP@DOXjade**. As mentioned in the introduction, cancer cells are known to have abnormal iron metabolism and are typically characterized by a relatively high dependence on iron (Fig. 5a). Certain forms of iron within the iron pool promote the growth of cancer cells by increasing reactive oxygen species, inducing DNA damage, regulating epigenetics and the transcription of oncogenic genes [10,49]. The "transferrin receptor" (TfR) plays an important role in iron uptake and iron metabolism. As shown in Fig. 5b–e, treatment of **Ti_3C_2-PVP@DOXjade** with 808 nm laser irradiation downregulated TfR expression compared with control groups consisting of ExHydra, DOX, **DOXjade**, and Ti_3C_2-PVP + 808 nm laser irradiation (Fig. 5b–e).

Several additional proteins that have a role in apoptosis, such as anti-apoptotic protein B-cell lymphoma 2 (Bcl-2) and the pro-apoptotic protein Bcl-2-associated X protein (Bax), were analyzed by Western blot assays. It was found that **Ti_3C_2-PVP@DOXjade** irradiated with 808 nm laser is more effective in inhibiting Bcl-2 expression than all other treatment groups (Fig. 5b and d). The pro-apoptotic protein Bax was also upregulated in the **Ti_3C_2-PVP@DOXjade** group relative to the other groups (Fig. 5b and e). On the basis of these findings, we conclude that iron chelation plays an important role in mediating the combined chemo- and photothermal therapeutic effect seen in the case of **Ti_3C_2-PVP@DOXjade**.

Conventional two-dimensional (2D) cell cultures are characterized by rapid and uncontrolled growth patterns, which are considered less accurate than three-dimensional (3D) tumor spheroids in mimicking *in vivo* tumor environment [50]. As a consequence, 3D culture modals are being used increasingly as a bridge between 2D monolayer experiments and animal studies [51]. The cytotoxicity of **Ti_3C_2-PVP@DOXjade** was thus further evaluated using 3D tumor spheroids. As can be seen from an inspection of Fig. 5f–h, statistically significant growth inhibition was seen in 3D tumor spheroids. Based on these data, we suggest that the combined treatment permitted by **Ti_3C_2-PVP@DOXjade** leads to an antitumor effect in accord with the mechanism given in Fig. 5a and that iron chelation can enhance the effects of conventional chemotherapy and PTT.

2.7. In vivo antitumor efficacy of Ti_3C_2-PVP@DOXjade

We next sought to assess the putative benefits of iron chelation coupled with chemo-photothermal therapy *in vivo* using a HCT116-based subcutaneous tumor mouse model. Prior to testing the ability of **Ti_3C_2-PVP@DOXjade** to inhibit tumor growth *in vivo*, hematological studies of Ti_3C_2-PVP were carried out to confirm its presumed biocompatibility. Previously, the biocompatibility of Ti_3C_2 modified with soybean phospholipids had been demonstrated [46]. We further tested the biocompatibility of Ti_3C_2-PVP in terms renal and liver function. Here, BALB/c mice were sacrificed after being subject to intravenous injection with Ti_3C_2-PVP on days 1, 7, and 14. Blood samples were collected and isolated by centrifugation in blood coagulation tubes to obtain the plasma. Evaluation of renal function was accomplished by quantifying urea and uric acid levels, while liver function was assessed by monitoring the total protein levels and albumin/globulin ratio in serum. Compared to the control group injected with saline, no significant renal toxicity or impairment of liver function was seen for Ti_3C_2-PVP (Fig. S9). These data provide support for the conclusion that Ti_3C_2-PVP is biocompatible.

Next, efficacy studies were carried out using HCT116 tumor-bearing nude mice. The mice were randomly divided into six groups (n = 5 per group), including (i) control group (saline), (ii) ExHydra group, (iii) DOX group, (iv) **DOXjade** group, (v) Ti_3C_2-PVP group with 808 nm laser irradiation and (vi) **Ti_3C_2-PVP@DOXjade** group with 808 nm laser irradiation. Six hours after intravenous administration of Ti_3C_2-PVP or **Ti_3C_2-PVP@DOXjade** to the tumor-bearing mice, the tumor site was directly irradiated with a NIR laser (808 nm, 1.0 W cm^{-2}, 10 min). In accord with our design expectation, a significant increase in tumor temperature was observed for the Ti_3C_2-PVP group (36.5–54.4 °C) (Fig. 6a and b). Monitoring the body weights of the animals in this cohort revealed no obvious changes or any observable adverse events (Fig. 6f). The Ti_3C_2-PVP group combined with 808 nm laser irradiation (1.0 W cm^{-2}, 10 min) achieved modest tumor growth inhibition; however, tumor reoccurrence was observed during the two-week study period (Fig. 6c and d). In contrast, **Ti_3C_2-PVP@DOXjade** combined with 808 nm laser irradiation achieved significant tumor eradication with no evidence of tumor regrowth over the course of the study (Fig. 6c and d).

To assess the tumor growth inhibition effects, immunohistochemical detection of the proliferation-associated antigen Ki67 was carried out. Ki67, a labile nuclear protein, has been reported as a valuable prognostic marker in colorectal cancer [52]. As shown in Fig. 6g, the Ki67 expression decreased in the **Ti_3C_2-PVP@DOXjade**-treated tumors compared with the other treatment groups. This reduction is consistent with the high antitumor activity **Ti_3C_2-PVP@DOXjade** provides under conditions of photo-irradiation.

3. Conclusion

In conclusion, here we proposed a "dual-therapeutic prodrug nanomedicine" approach for iron chelation chemo-photothermal therapy. Especially, to realize this goal, a new and novel tumoral acidic microenvironment responsive dual-therapeutic conjugate **DOXjade** that incorporates in the clinically approved iron chelator deferasirox and DOX was rationally designed. After loading onto the engineered ultrathin 2D Ti_3C_2 MXene nanosheets, resulting **Ti_3C_2-PVP@DOXjade** not only enables the inherent iron chelation and chemotherapeutic functions of **DOXjade** to be selectively activated at the tumor sites, but imparts a robust photothermal potential with the photothermal conversion efficiency up to 40%. Remarkably, **Ti_3C_2-PVP@DOXjade** also displays an outstanding drug loading efficiency. Antitumor mechanism investigations reveal the iron depletion-induced TfR protein down-regulation and apoptotic cell death under multimodal treatments. With these unique merits, sensitive tumor pH-responsive iron chelation/PTT/chemotherapy antitumor effect was achieved both *in vitro* and *in vivo*. This study therefore represents a promising iron chelation phototherapeutic paradigm toward cancer precise therapy.

CRediT authorship contribution statement

Yunjie Xu: Project administration, Conceptualization, Data curation, Investigation, Software, Formal analysis, Writing – original draft. **Yingwei Wang:** Investigation, Data curation, Resources, Writing – original draft, Funding acquisition. **Jusung An:** Investigation, Data curation, Formal analysis. **Adam C. Sedgwick:** Investigation, Resources, Data curation, Formal analysis, Writing – review & editing. **Mingle Li:** Writing – review & editing, Funding acquisition. **Jianlei Xie:** Methodology. **Weibin Hu:** Methodology. **Jianlong Kang:** Investigation. **Sajal Sen:** Investigation, Writing – review & editing. **Axel Steinbrueck:** Investigation, Writing – review & editing. **Bin Zhang:** Methodology. **Lijun Qiao:** Methodology. **Swelm Wageh:** Methodology, Writing – review & editing. **Jonathan F. Arambula:** Supervision, Writing – review & editing. **Liping Liu:** Supervision. **Han Zhang:** Conceptualization, Supervision. **Jonathan L. Sessler:** Project administration, Conceptualization, Supervision, Funding acquisition, Writing – review & editing. **Jong Seung Kim:** Project administration, Conceptualization, Supervision, Funding acquisition, Writing – review & editing.

Declaration of competing interest

The authors declare no conflict of interest.

Acknowledgements

This work was supported by the National Natural Science Foundation of China (Grant No. 11904239, Y.W.W) and the Creative Research Initiative of National Research Foundation of Korea (NRF) (CRI project No. 2018R1A3B1052702, J.S.K.). Initial support for the work in Austin came from the National Institutes of Health (CA 68682 to J.L.S.) with subsequent funding from the Robert A. Welch Foundation (F-0018 to J. L.S.). This work was supported by Brain Pool Program through the funded by the Ministry of Science and ICT (Grant No. 2020H1D3A1A02080172, M.L.).

Appendix A. Supplementary data

Supplementary data to this article can be found online at https://doi.org/10.1016/j.bioactmat.2021.12.011.

References

[1] S. Pilleron, E. Soto-Perez-de-Celis, J. Vignat, J. Ferlay, I. Soerjomataram, F. Bray, et al., Estimated global cancer incidence in the oldest adults in 2018 and projections to 2050, Int. J. Cancer 148 (3) (2021) 601–608.
[2] J. Ferlay, M. Colombet, I. Soerjomataram, D.M. Parkin, M. Piñeros, A. Znaor, et al., Cancer statistics for the year 2020: an overview, Int. J. Cancer 149 (4) (2021) 778–789.
[3] H. Sung, J. Ferlay, R.L. Siegel, M. Laversanne, I. Soerjomataram, A. Jemal, et al., Global cancer statistics 2020: GLOBOCAN estimates of incidence and mortality worldwide for 36 cancers in 185 countries, CA A Cancer J. Clin. 71 (3) (2021) 209–249.
[4] W.D. Tap, R.L. Jones, B.A. Van Tine, B. Chmielowski, A.D. Elias, D. Adkins, et al., Olaratumab and doxorubicin versus doxorubicin alone for treatment of soft-tissue sarcoma: an open-label phase 1b and randomised phase 2 trial, Lancet 388 (10043) (2016) 488–497.
[5] M.T. Nuñez, P. Chana-Cuevas, New perspectives in iron chelation therapy for the treatment of neurodegenerative diseases, Pharmaceuticals 11 (4) (2018).
[6] E. Poggiali, E. Cassinerio, L. Zanaboni, M.D. Cappellini, An update on iron chelation therapy, Blood Transfus 10 (4) (2012) 411–422.
[7] A. Steinbrueck, A.C. Sedgwick, J.T. Brewster, K.-C. Yan, Y. Shang, D.M. Knoll, et al., Transition metal chelators, pro-chelators, and ionophores as small molecule cancer chemotherapeutic agents, Chem. Soc. Rev. 49 (12) (2020) 3726–3747.
[8] P. Aisen, C. Enns, M. Wessling-Resnick, Chemistry and biology of eukaryotic iron metabolism, Int. J. Biochem. Cell Biol. 33 (10) (2001) 940–959.
[9] S. Lakhal-Littleton, Ferroportin mediated control of iron metabolism and disease, Blood 128 (22) (2016). SCI-21-SCI-21.

[10] D.R. Richardson, D.S. Kalinowski, S. Lau, P.J. Jansson, D.B. Lovejoy, Cancer cell iron metabolism and the development of potent iron chelators as anti-tumour agents, BBA-Gen. Subjects 1790 (7) (2009) 702–717.
[11] S.V. Torti, F.M. Torti, Iron and cancer: more ore to be mined, Nat. Rev. Cancer 13 (5) (2013) 342–355.
[12] S. Tury, F. Assayag, F. Bonin, S. Chateau-Joubert, J.-L. Servely, S. Vacher, et al., The iron chelator deferasirox synergises with chemotherapy to treat triple-negative breast cancers, J. Pathol. 246 (1) (2018) 103–114.
[13] G.Y.L. Lui, P. Obeidy, S.J. Ford, C. Tselepis, D.M. Sharp, P.J. Jansson, et al., The iron chelator, deferasirox, as a novel strategy for cancer treatment: oral activity against human lung tumor xenografts and molecular mechanism of action, Mol. Pharmacol. 83 (1) (2013) 179.
[14] A. Steinbrueck, A.C. Sedgwick, H.-H. Han, M.Y. Zhao, S. Sen, D.-Y. Huang, et al., In vitro studies of deferasirox derivatives as potential organelle-targeting traceable anti-cancer therapeutics, Chem. Commun. 57 (46) (2021) 5678–5681.
[15] J.D. Díaz-García, A. Gallegos-Villalobos, L. Gonzalez-Espinoza, M.D. Sanchez-Niño, J. Villarrubia, A. Ortiz, Deferasirox nephrotoxicity–the knowns and unknowns, Nat. Rev. Nephrol. 10 (10) (2014) 574–586.
[16] S. Shinoda, S. Kaino, S. Amano, H. Harima, T. Matsumoto, K. Fujisawa, et al., Deferasirox, an oral iron chelator, with gemcitabine synergistically inhibits pancreatic cancer cell growth in vitro and in vivo, Oncotarget 9 (47) (2018).
[17] W. Fan, B. Yung, P. Huang, X. Chen, Nanotechnology for multimodal synergistic cancer therapy, Chem. Rev. 117 (22) (2017) 13566–13638.
[18] P. Liang, B. Ballou, X. Lv, W. Si, M.P. Bruchez, W. Huang, et al., Monotherapy and combination therapy using anti-angiogenic nanoagents to fight cancer, Adv. Mater. 33 (15) (2021) 2005155.
[19] Powerful combination therapies, Nat. Biomed. Eng. 2 (8) (2018) 555–556.
[20] J.H. Doroshow, R.M. Simon, On the design of combination cancer therapy, Cell 171 (7) (2017) 1476–1478.
[21] J.-L. Liang, G.-F. Luo, W.-H. Chen, X.-Z. Zhang, Recent advances in engineered materials for immunotherapy–involved combination cancer therapy, Adv. Mater. 33 (31) (2021) 2007630.
[22] H.S. Jung, P. Verwilst, A. Sharma, J. Shin, J.L. Sessler, J.S. Kim, Organic molecule–based photothermal agents: an expanding photothermal therapy universe, Chem. Soc. Rev. 47 (7) (2018) 2280–2297.
[23] Y. Liu, P. Bhattarai, Z. Dai, X. Chen, Photothermal therapy and photoacoustic imaging via nanotheranostics in fighting cancer, Chem. Soc. Rev. 48 (7) (2019) 2053–2108.
[24] H. Zhou, X. Zeng, A. Li, W. Zhou, L. Tang, W. Hu, et al., Upconversion NIR-II fluorophores for mitochondria-targeted cancer imaging and photothermal therapy, Nat. Commun. 11 (1) (2020) 6183.
[25] Y. Zheng, Q. Li, J. Wu, Z. Luo, W. Zhou, A. Li, et al., All-in-one mitochondria-targeted NIR-II fluorophores for cancer therapy and imaging, Chem. Sci. 12 (5) (2021) 1843–1850.
[26] X. Zeng, Y. Xiao, J. Lin, S. Li, H. Zhou, J. Nong, et al., Near-infrared II dye-protein complex for biomedical imaging and imaging-guided photothermal therapy, Adv. Healthc. Mater. 7 (18) (2018) 1800589.
[27] K. Hu, L. Xie, Y. Zhang, M. Hanyu, Z. Yang, K. Nagatsu, et al., Marriage of black phosphorus and Cu^{2+} as effective photothermal agents for PET-guided combination cancer therapy, Nat. Commun. 11 (1) (2020) 2778.
[28] W. Huang, Y. Huang, Y. You, T. Nie, T. Chen, High-yield synthesis of multifunctional tellurium nanorods to achieve simultaneous chemo-photothermal combination cancer therapy, Adv. Funct. Mater. 27 (33) (2017) 1701388.
[29] J. Li, L. Xie, B. Li, C. Yin, G. Wang, W. Sang, et al., Engineering a hydrogen-sulfide-based nanomodulator to normalize hyperactive photothermal immunogenicity for combination cancer therapy, Adv. Mater. 33 (22) (2021) 2008481.
[30] C. Xu, K. Pu, Second near-infrared photothermal materials for combinational nanotheranostics, Chem. Soc. Rev. 50 (2) (2021) 1111–1137.
[31] K. Huang, Z. Li, J. Lin, G. Han, P. Huang, Two-dimensional transition metal carbides and nitrides (MXenes) for biomedical applications, Chem. Soc. Rev. 47 (14) (2018) 5109–5124.
[32] H. Lin, Y. Chen, J. Shi, Insights into 2D MXenes for versatile biomedical applications: current advances and challenges ahead, Adv. Sci. 5 (10) (2018) 1800518.
[33] Y. Wang, M. Qiu, M. Won, E. Jung, T. Fan, N. Xie, et al., Emerging 2D material-based nanocarrier for cancer therapy beyond graphene, Coord. Chem. Rev. 400 (2019) 213041.
[34] J. Ouyang, X. Ji, X. Zhang, C. Feng, Z. Tang, N. Kong, et al., In situ sprayed NIR-responsive, analgesic black phosphorus-based gel for diabetic ulcer treatment, Proc. Natl. Acad. Sci. U.S.A. 117 (46) (2020) 28667–28677.
[35] J. Ouyang, C. Feng, X. Ji, L. Li, H.K. Gutti, N.Y. Kim, et al., 2D monoelemental germanene quantum dots: synthesis as robust photothermal agents for photonic cancer nanomedicine, Angew. Chem. Int. Ed. 58 (38) (2019) 13405–13410.
[36] J. Ouyang, C. Feng, X. Zhang, N. Kong, W. Tao, Black phosphorus in biological applications: evolutionary journey from monoelemental materials to composite materials, Acc. Chem. Res. 2 (7) (2021) 489–500.
[37] H. Lin, X. Wang, L. Yu, Y. Chen, J. Shi, Two-dimensional ultrathin MXene ceramic nanosheets for photothermal conversion, Nano Lett. 17 (1) (2017) 384–391.
[38] M. Li, Y. Shao, J.H. Kim, Z. Pu, X. Zhao, H. Huang, et al., Unimolecular photodynamic O_2-economizer to overcome hypoxia resistance in phototherapeutics, J. Am. Chem. Soc. 142 (11) (2021) 5380–5388.
[39] M. Li, T. Xiong, J. Du, R. Tian, M. Xiao, L. Guo, et al., Superoxide radical photogenerator with amplification effect: surmounting the Achilles' Heels of photodynamic oncotherapy, J. Am. Chem. Soc. 141 (6) (2019) 2695–2702.
[40] M. Naguib, M. Kurtoglu, V. Presser, J. Lu, J. Niu, M. Heon, et al., Two-dimensional nanocrystals produced by exfoliation of Ti_3AlC_2, Adv. Mater. 23 (37) (2011) 4248–4253.
[41] X. Jiang, S. Liu, W. Liang, S. Luo, Z. He, Y. Ge, et al., Broadband nonlinear photonics in few-layer MXene Ti_3C_2Tx (T = F, O, or OH), Laser Photon. Rev. 12 (2) (2018) 1870013.
[42] C.E. Shuck, A. Sarycheva, M. Anayee, A. Levitt, Y. Zhu, S. Uzun, et al., Scalable synthesis of Ti_3C_2Tx MXene, Adv. Eng. Mater. 22 (3) (2020) 1901241.
[43] B. Anasori, M.R. Lukatskaya, Y. Gogotsi, 2D metal carbides and nitrides (MXenes) for energy storage, Nat. Rev. Mater. 2 (2) (2017) 16098.
[44] B. Anasori, C. Shi, E.J. Moon, Y. Xie, C.A. Voigt, P.R.C. Kent, et al., Control of electronic properties of 2D carbides (MXenes) by manipulating their transition metal layers, Nanoscale Horiz 1 (3) (2016) 227–234.
[45] T. Fukushima, H. Kawabata, T. Nakamura, H. Iwao, A. Nakajima, M. Miki, et al., Iron chelation therapy with deferasirox induced complete remission in a patient with chemotherapy-resistant acute monocytic leukemia, Anticancer Res. 31 (5) (2011) 1741.
[46] X. Han, J. Huang, H. Lin, Z. Wang, P. Li, Y. Chen, 2D ultrathin MXene-based drug-delivery nanoplatform for synergistic photothermal ablation and chemotherapy of cancer, Adv. Healthc. Mater. 7 (9) (2018) 1701394.
[47] M. Li, S. Long, Y. Kang, L. Guo, J. Wang, J. Fan, et al., De novo design of phototheranostic sensitizers based on structure-inherent targeting for enhanced cancer ablation, J. Am. Chem. Soc. 140 (46) (2018) 15820–15826.
[48] M. Li, J. Xia, R. Tian, J. Wang, J. Fan, J. Du, et al., Near-infrared light-initiated molecular superoxide radical generator: rejuvenating photodynamic therapy against hypoxic tumors, J. Am. Chem. Soc. 140 (44) (2018) 14851–14859.
[49] L.S. Schneider, K. von Schwarzenberg, T. Lehr, M. Ulrich, R. Kubisch-Dohmen, J. Liebl, et al., Vacuolar-ATPase inhibition blocks iron metabolism to mediate therapeutic effects in breast cancer, Cancer Res. 75 (14) (2015) 2863.
[50] G.Y. Lee, P.A. Kenny, E.H. Lee, M.J. Bissell, Three-dimensional culture models of normal and malignant breast epithelial cells, Nat. Methods 4 (4) (2007) 359–365.
[51] J. Friedrich, C. Seidel, R. Ebner, L.A. Kunz-Schughart, Spheroid-based drug screen: considerations and practical approach, Nat. Protoc. 4 (3) (2009) 309–324.
[52] G. Tong, G. Zhang, J. Liu, Z. Zheng, Y. Chen, P. Niu, et al., Cutoff of 25% for Ki67 expression is a good classification tool for prognosis in colorectal cancer in the AJCC-8 stratification, Oncol. Rep. 43 (4) (2020) 1187–1198.